RESEARCH ARTICLE

Efficient Synthetic Aperture for Phaseless Fourier Ptychographic Microscopy with Hybrid Coherent and Incoherent Illumination

Yao Fan, Jiasong Sun, Yefeng Shu, Zuxin Zhang, Guoan Zheng, Wenjian Chen, Jin Zhang, Kun Gui, Kehui Wang, Qian Chen,* and Chao Zuo*

Fourier ptychographic microscopy (FPM) is a computational high-throughput technique for high-resolution and wide field-of-view (FOV) imaging applications such as cell biology, medicine screening, and digital pathology. By integrating angle-varied illumination, iteration phase retrieval, and synthetic aperture, it achieves a significantly enhanced imaging resolution beyond the diffraction limit of the objective lens while retaining its original large FOV without any mechanical movement. However, sufficient data redundancy is a prerequisite for the convergence of the iteration algorithm, which in turn requires dozens or even hundreds of raw images to get a decent resolution, leaving ample room for further improvement. In this paper, an efficient synthetic aperture scheme for FPM is proposed, termed ESA-FPM. It employs both coherent and incoherent illuminations to maximize the efficiency of data utilization and achieve high spatial-bandwidth product (SBP) reconstruction with few acquisitions. The data redundancy requirements are further analyzed, suggesting that ESA-FPM reaches imaging resolution of $3NA_{obj}$ using only seven images. The experiment with USAF target demonstrates that ESA-FPM achieves theoretical resolution with only 1.6% of the data of conventional FPM. A customized miniaturized ESA-FPM system with a high-numerical-aperture, low-magnification objective lens, and a high-brightness LED array is built, demonstrating its potential for biomedical and pathological applications.

1. Introduction

High-throughput imaging is essential for many biomedical applications, such as cell monitoring,[1] drug screening,[2] and diagnostic pathology.[3] In particular, digital pathology requires high-resolution and large-scale "digital slides" to identify the cause of diseases based on morphologic findings and related auxiliary tests.[4] Its touchstone is the histologic appearance of diseased and normal tissues when stained with conventional stains (usually hematoxylin and eosin). An ideal imaging technique should be able to image the stained histology slide with cellular or subcellular scale resolution across a large field-of-view (FOV).[5] The imaging throughput of traditional optical platforms, however, follows the well-known law of Lagrange invariant,[6] imposing an unavoidable trade-off between imaging resolution and FOV. Whole slide imaging (WSI), also referred to as "virtual microscopy," is the common high-throughput imaging method for diagnostic pathology.[4,7] It utilizes specialized hardware (scanner) to digitize pathology slides, generating a large representative "digital slide." In essence, it integrates the capabilities of the high-resolution imaging of the high-magnification objective lens and the FOV scanning of the high-precision optical displacement platform (with micron or even nanoscale). The resulting image is a comprehensive digital rendering of an entire microscope slide, visible at a resolution of less than 1 μm, allowing the entire slide to be available for

Y. Fan, J. Sun, Y. Shu, Z. Zhang, W. Chen, Q. Chen, C. Zuo
Smart Computational Imaging (SCI) Laboratory
Nanjing University of Science and Technology
Nanjing, Jiangsu Province 210094, China
E-mail: chenqian@njust.edu.cn; zuochao@njust.edu.cn
Y. Fan, J. Sun, Y. Shu, Z. Zhang, W. Chen, Q. Chen, C. Zuo
Smart Computational Imaging Research Institute (SCRI), Nanjing
University of Science and Technology
Nanjing, Jiangsu Province 210019, China

Y. Fan, J. Sun, Y. Shu, Z. Zhang, W. Chen, Q. Chen, C. Zuo
Jiangsu Key Laboratory of Spectral Imaging and Intelligent Sense
Nanjing University of Science and Technology
Nanjing, Jiangsu Province 210094, China
G. Zheng
Department of Biomedical Engineering
University of Connecticut
Storrs, CT 06269, USA
J. Zhang
Ningbo Diagnostic Pathology Center
Ningbo, Zhejiang Province 315021, China
K. Gui, K. Wang
Konfoong Biotech International Co., LTD
Yuyao, Zhejiang Province 315400, China

analysis. However, its complex hardware configuration leads to an expensive, bulky, and highly specialized design, which hinders its widespread application in pathology diagnosis. Moreover, while the imaging speed and quality of WSI are continuously improving with the advance in high-performance optics and mechanics, acquiring consistently well-focused images across the whole slide remains a major challenge.

Recent advances in optical modulation mechanisms and computational imaging algorithms have overcome many physical limitations of traditional optical microscopy, promoting the pioneering progress of microscopic imaging techniques. Many emerging computational imaging technologies were developed, such as differential phase contrast imaging,[8–10] quantitative phase imaging,[11–18] high-throughput imaging,[19–23] refractive index diffraction tomography,[24,25] etc. These technologies provide unique optical imaging capabilities for various biological and medical applications.[26–29] Computational high-throughput microscopic techniques allow for both high-resolution and large-FOV imaging without involving mechanical scanning, providing an attractive alternative to traditional spatial stitching (WSI) techniques. Fourier ptychographic microscopy (FPM), a promising high-throughput computational imaging technique, obtains high-resolution details comparable to that of the high-numerical-aperture (high-NA)objective lens while retaining the original large FOV of the low-NA objective lens without involving mechanical scanning.[19,30] It uses angular illumination scanning to record sample information of different spatial frequency contents. This can be easily implemented by replacing the illumination source of the microscope with a programmable LED array, and thus, it is compatible with most microscope platforms in laboratories. In the acquisition process, each LED unit element is turned on to produce a plane wave with a certain incident angle. By sequentially illuminating the sample from different incident angles, it records a series of low-resolution and wide FOV images for subsequent iteration reconstruction. By synthesizing these images in the corresponding regions in the reciprocal space, FPM is able to achieve significantly improved spatial resolution beyond the diffraction limit of the objective lens. Conclusively, the equivalent NA can be extended to the sum of the objective NA and the illumination NA. In addition, the large depth of field (DOF) of the low-NA objective lens effectively addresses the difficulty of autofocusing process in conventional WSI platforms. Due to its simple hardware configuration and improved imaging performance, FPM has found wide-ranging biomedical and pathologic applications, such as circulating tumor cells cytometry,[31] white blood cell count,[32] and high-content screening.[33]

Originating from the concept of ptychographic phase retrieval,[34,35] FPM iteratively switches between the real and reciprocal spaces to recover the lost sample information.[34,36–41] Such a reconstruction process can be considered as solving an optimization problem, where a certain amount of data redundancy is required to ensure the stable convergence of the iteration process.[42] This requirement can be met by dense illumination sampling at the expense of a large number of image acquisitions and a significant reduction in imaging efficiency. In particular, this not only prolongs the acquisition time (especially for dark-field images that require long exposure times to ensure

adequate signal-to-noise ratio) but also complicates the data processing process. In order to address this problem, some efforts have been made to improve the FPM imaging efficiency by reducing the number of data acquisitions.[43–48] On the one hand, illumination multiplexing was exploited in FPM to acquire multiple sub-aperture image information simultaneously with a single exposure, accelerating the data acquisition and spectrum filling.[44,49] However, due to the complex decoherence process involved, the data redundancy requirement is increased proportionally with the number of multiplexed modes, creating additional risks of "incomplete demultiplexing artifacts." On the other hand, the sparse sampling strategy was proposed to reduce the acquired data by making full use of the minimum spectrum overlapping requirement for which the FPM iteration can converge.[45,50] Specifically, all sub-aperture spectrums are sparsely sampled with a spectrum overlapping percentage of no less than 40%. Although these strategies can improve the data acquisition efficiency of FPM to a certain extent, they still generally require tens of frames of raw data to achieve a decent reconstruction, leaving ample room for further improvement. Therefore, maximizing the efficiency of data utilization and achieving high spatial-bandwidth product (SBP) reconstruction with few frames is a key aspect to promote wider applications of FPM in biomedicine and pathology.

In this paper, we propose an efficient synthetic aperture scheme for FPM, termed ESA-FPM. In its implementation, the sequentially coherent illumination is replaced by a new hybrid illumination scheme, which integrates both the incoherent (bright-field) and coherent (dark-field) imaging to significantly improve the data efficiency and shorten the algorithm time by several orders of magnitude. In bright-field acquisition, all LEDs are turned on simultaneously as an extended light source to collect a single intensity image under incoherent illumination. Such a single bright-field intensity is filtered by the optical transfer function (OTF) and then iteratively enforced in the synthetic spectrum, thus generating a spectrum coverage with the 2× bandwidth of coherent diffraction limit. Dark-field image acquisition is based on centrosymmetric sparse sampling for further resolution enhancement. The similarity of image information under centrosymmetric illumination is demonstrated and used to establish an accelerated image acquisition and iteration update scheme. Furthermore, we analyze the data redundancy and explore the most efficient hybrid illumination scheme for ESA-FPM, thus achieving an imaging resolution of 3× the coherent diffraction limit with only seven original images. As a result, all acquired data is fully contributed to the final reconstructed result without any encumbrance. We demonstrate the imaging resolution of ESA-FPM based on a standard FPM platform using a standard resolution target, verifying that the theoretical imaging resolution can be reached despite using only 1.6% of the conventional FPM acquisition data. For the implementation of pathological diagnostic applications, we design and construct a miniaturized ESA-FPM system with a customized high-NA, wide-FOV objective lens and high-brightness LED, achieving a synthesized NA of 1.05 over a wide imaging FOV of 2.19×1.46 mm^2. Experimental results on pathology slides suggest that ESA-FPM can provide an efficient high-throughput imaging solution for rapid digital pathology.
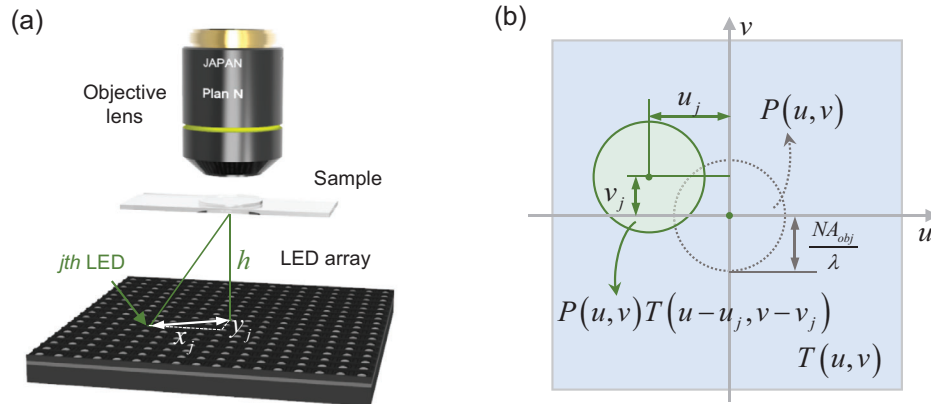
Figure 1. A typical FPM system adopts a programmable LED array to generate angle-varied plane illumination without any moving parts. a) Schematic diagram of jth LED. b) The confined pupil aperture with shift frequency of u_j, v_j.

2. Algorithm Model of FPM

A typical FPM system is built by replacing the light source of the traditional microscope with a programmable LED array.[19,51] All LED units can be independently controlled to generate angle-varied plane illumination without any moving parts. Considering a standard FPM optical setup, the LED elements are sequentially turned on for angle-varied illumination and acquire the images using a low-NA objective lens. In the Fourier space, these illuminations effectively pan the confined pupil aperture at the Fourier domain, enabling substantial resolution enhancement beyond what is limited by the pupil aperture. The image generation model for this process can be described by the following mathematical expression. Assuming a sample with complex transmittance function of $t(x, y) = e^{a(x,y)+i\phi(x,y)}$ (x, y denote the spatial coordinates, $a(x, y)$ denotes the absorption distribution, and $\phi(x, y)$ is the phase distribution) is illuminated by a single LED with shift frequency of (u_j, v_j), as shown in **Figure 1**, the intensity distribution in the camera plane can be expressed as the result of the intensity distribution corresponding to the sample complex distribution filtered by the coherent transfer function (CTF)

$$I_j(x, y) = |\mathscr{F}^{-1}\{\text{CTF}(u, v)T(u - u_j, v - v_j)\}|^2 \quad (1)$$

where $\mathscr{F}^{-1}\{\cdot\}$ is the inverse Fourier transform operation. (u, v) denotes the spatial frequency coordinates in the Fourier domain. In a system without aberrations, $\text{CTF}(u, v)$ is considered as the pupil function of the objective lens $P(u, v)$, which is a low-pass filter function with a cutoff frequency of $\frac{\text{NA}_{obj}}{\lambda}$ (NA_{obj} is the NA of the objective lens, and λ is the illumination wavelength). Each angular illumination will determine a unique spatial frequency coordinate (u_j, v_j) (Figure 1b), which defines the filtering center frequency corresponding to jth illumination, and they can be determined by the following equation

$$u_j = \frac{x_j - x_o}{\lambda\sqrt{(x_j - x_o)^2 + (y_j - y_o)^2 + h^2}},$$

$$v_j = \frac{y_j - y_o}{\lambda\sqrt{(x_j - x_o)^2 + (y_j - y_o)^2 + h^2}} \quad (2)$$

From Figure 1a, x_j, y_j are the lateral distances of the jth LED unit from the center LED on the optical axis, x_o, y_o are the distances between the current object plane coordinates and the center point, and h indicates the height between the carrier table where the sample is placed and the LED array. According to the relationship between spatial frequencies of u_j, v_j, and the cut-off frequency of objective lens $\frac{\text{NA}_{obj}}{\lambda}$, the captured images can be distinguished between bright-field and dark-field imaging

$$\begin{cases} \sqrt{(u_j)^2 + (v_j)^2} \leq \frac{\text{NA}_{obj}}{\lambda}, & \text{bright field} \\ \sqrt{(u_j)^2 + (v_j)^2} > \frac{\text{NA}_{obj}}{\lambda}, & \text{dark field} \end{cases} \quad (3)$$

This equation implies that the sub-aperture spectrum of the bright-field illumination contains the zero-frequency component, while dark-field illumination moves low-frequency components beyond the captured sub-aperture spectrum. Thus, the bright-field image records the low-frequency information of the sample under transmittance light, and the dark-field image collects the high-resolution scattering information under large-angle tilt illumination. Therefore, the original acquisitions present information about the sample at different spatial frequencies.

These shifted sub-aperture spectrums are synthesized in the Fourier domain by iteration reconstruction to bypass the diffraction limit of the objective lens. The solution of this process is recovered by the alternating projection (AP) algorithm,[34,36–38] that is, the estimated solution is alternatively projected to two constraint sets in the spatial and Fourier domains. In the spatial domain, the collected intensity is used as an amplitude constraint, while in the Fourier domain, the finite sub-aperture is used as a support domain constraint. For each illumination angle, the sub-aperture spectrum is extracted for inverse Fourier transform, and its amplitude distribution is updated by the acquired intensity information. This updated complex amplitude distribution is then transformed to the Fourier domain and confined by CTF, and finally shifted by the illumination vector (u_j, v_j). The successive iterations will eventually reach a stable solution that the constraints resulting from the overlapping condition and the intensity measurements can be satisfied simultaneously. As a result,
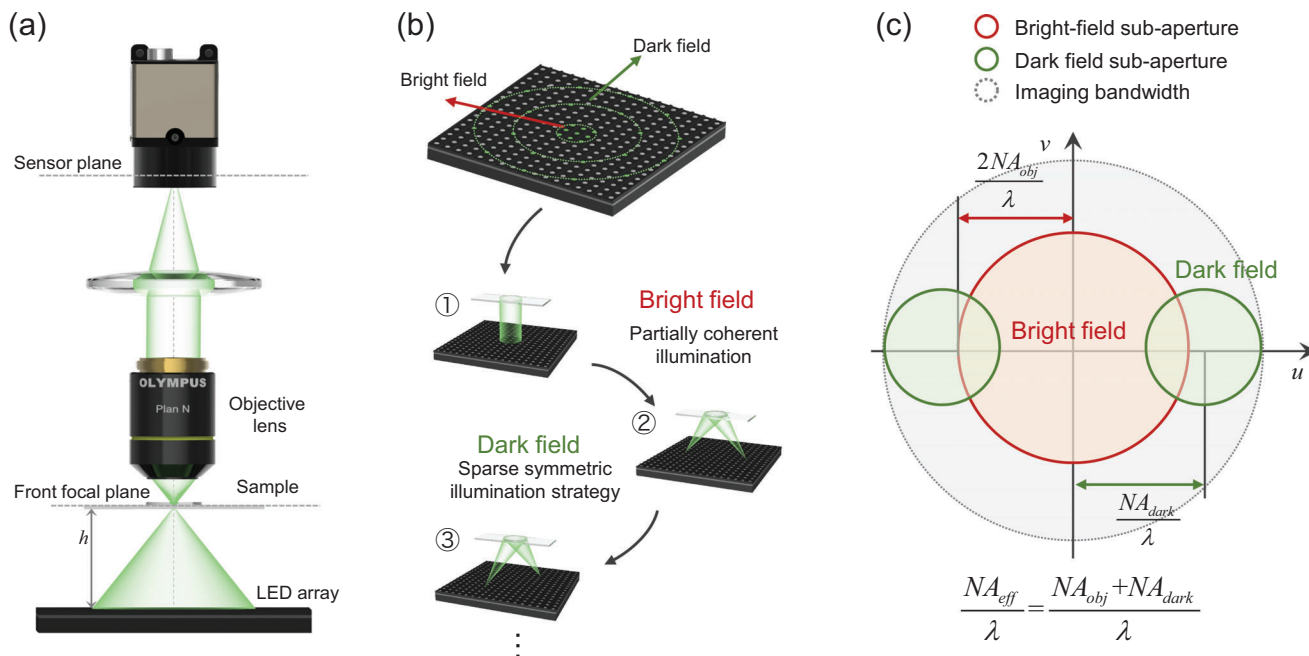
Figure 2. Hybrid illumination modes of ESA-FPM. a) ESA-FPM imaging system. b) Hybrid illumination modes that distinguish between bright field and dark field. c) The spectrum filling model of hybrid illumination modes.

the "lost" information is recovered by updating functions back and forth between the spatial and Fourier spaces with captured low-resolution images. The solution of FPM can be formulated as a non-convex optimization problem[52,53]

$$\min_{T(u,v)} \sum_{j} \sum_{x,y} \left| \sqrt{I_j(x,y)} - \left| \mathscr{F}^{-1}\{P(u,v)\,T(u-u_j, v-v_j)\} \right| \right|^2 \quad (4)$$

The final effective NA will reach the sum of the objective NA_{obj} and the illumination NA_{ill}, ($NA_{eff} = NA_{obj} + NA_{ill}$), leading to an imaging resolution $\frac{\lambda}{(NA_{obj}+NA_{ill})}$ (full-pitch resolution) beyond the diffraction limit of the objective lens. In addition, since the raw images are captured through a low-magnification objective lens, the final reconstruction retains a wide FOV and long DOF.

However, although FPM achieves both high resolution and wide FOV, this is at the expense of efficiency consumption. A spectrum overlapping percentage of not less than 40% is required to ensure data redundancy.[45,50] For this purpose, dense illumination sampling is usually employed in FPM, but this produces a huge dataset (on the order of gigapixels), which is synthesized in the final reconstruction results with very low efficiency. Moreover, image recording requires a long exposure time, especially for dark-field images that record scattering signals with very weak intensities and require longer exposure times to allow them to be acquired with an adequate signal-to-noise ratio. For example, to obtain an effective imaging NA of $3NA_{obj}$, the maximum illumination NA_{ill} of the illumination scanning should be designed to be twice the NA of the objective lens. Assuming a general FPM system configured with an objective lens with NA_{obj} of 0.25, and an LED array with a spacing of 4 mm is placed 74 mm below the sample for illumination. To generate the maximum illumination

$NA_{ill} = 2NA_{obj}$, the distance between the LEDs of the maximum illumination NA and the center LED must be no less than 40 mm. As a result, at least 400 low-resolution images (89 bright-field and 352 dark-field images) must be recorded to guarantee the success of the FPM iteration algorithm.

3. Method

3.1. Hybrid Coherent/Incoherent Illumination Scheme

To address the mentioned problem, we propose ESA-FPM and explore its maximum data cost efficiency for efficient high-throughput imaging applications. In ESA-FPM, a hybrid incoherent/coherent illumination scheme and the corresponding iteration algorithm that distinguish between bright field and dark field based on their image formation properties are proposed, as shown in **Figure 2**. Unlike the traditional FPM, whose LEDs are lit sequentially to produce spatially coherent illumination, all LED units within bright-field illumination are turned on simultaneously in ESA-FPM to illuminate the sample in an incoherent manner (Figure 2b), acquiring a single bright-field image. Such a decoherent illumination is considered an undesired case in conventional FPM and is attempted to be handled by spectral demultiplexing algorithms or replacing the LED array with a highly coherent light source.[43,46] In ESA-FPM, we modified the iteration algorithm according to the spatial coherence of the illumination so that the superiority of incoherent illumination can be exploited to improve the imaging robustness and accelerate the image efficiency. According to the theory of coherent mode decomposition,[54] the acquired intensity under such incoherent illumination can be equated as a linear superposition of the intensity of different coherent states. This means that a single

ADVANCED
SCIENCE NEWS
www.advancedsciencenews.com

LASER
& PHOTONICS
REVIEWS
www.lpr-journal.org

bright-field image almost contains all the spatial frequency information of samples within the incoherent diffraction bandwidth. Thus, the traditionally considered coherent imaging of FPM is transformed into the incoherent imaging model, which is linear with intensity

$$I_{BF}(u, v) = OTF(u, v) \times I_T(u, v) \qquad (5)$$

where $I_{BF}(u, v)$ is the intensity spectrum of bright-field acquisition and $I_T(u, v)$ is the ideal intensity spectrum distribution of the sample. $OTF(u, v)$ is the optical transfer function (OTF), which is defined as the normalized autocorrelation of the CTF (pupil function, $P(u, v)$) to characterize the filtering performance of the imaging system to the recorded intensity

$$OTF(u, v) = P(u, v) \star P(u, v)|_{norm}$$
$$= \frac{\iint P(u, v) P^*(u - \tilde{u}, v - \tilde{v}) \mathrm{d}\tilde{u}\mathrm{d}\tilde{v}}{\iint |P(\tilde{u}, \tilde{v})|^2 \mathrm{d}\tilde{u}\mathrm{d}\tilde{v}} \qquad (6)$$

where $\star$ indicates a correlation, and $\cdot|_{norm}$ is the normalization operation. All spatial frequencies in incoherent imaging bandwidth (twice the imaging bandwidth of the coherent diffraction limit of the objective lens) are filtered by the OTF transfer response and finally presented in the collected intensity signal. It should be mentioned that the transfer response of OTF is no longer uniformly distributed like CTF, but decays with the increase of spatial frequency until it decays to 0 at $\frac{2NA_{obj}}{\lambda}$.[55] This indicates the theoretical resolution of bright-field imaging is unattainable. To enhance the imaging contrast of the high-frequency details, we implement a deconvolution by the bright-field intensity spectrum with the OTF of the system to initialize the high-resolution spectrum. Therefore, the coverage spectrum within $\frac{2NA_{obj}}{\lambda}$ will be recovered by one inversion solution, which will serve as the basis for subsequent iterations.

The dark-field acquisition is implemented by a centrosymmetric sparse illumination, which ensures large illumination NA as well as a minimum number of illumination angle images. As shown in Figure 2b, the illumination pattern is a series of discrete LEDs, which are uniformly distributed in an annulus with the radius of NA_{dark} (the illumination NAs of these LEDs are larger than the NA of the objective, that is, $NA_{dark} > NA_{obj}$). These LEDs produce tilted illuminations with different azimuths but equal illumination NA. All these discrete LEDs are required to meet the spectrum overlapping percentage while eliminating data redundancy. For each acquisition, a centrosymmetric pair of LEDs (with the frequency shifts of (u_j, v_j) and $(-u_j, -v_j)$) are turned on simultaneously to acquire a dark-field image. Based on the symmetry of the spectrum information of weak objects, it can be theoretically derived that the centrosymmetric dark-field illuminations can acquire the same intensity signal. Furthermore, the phase of the sample is almost cancelled out, leaving only the absorption distribution of the sample $A(u, v)$ in the acquisition intensity

$$I_{u_j,v_j}(u, v) + I_{-u_j,-v_j}(u, v) \approx 2[A(u - u_j, v - v_j) P(u, v)]$$
$$\otimes [A(u + u_j, v + v_j) P(u, v)] \qquad (7)$$

The derivation and simulation verification of Equation (7) can be found in Appendix. Each captured intensity image in ESA-FPM can be used to directly update both sub-apertures under centrosymmetric illuminations without information demultiplexing. Consequently, the centrosymmetric dark-field illumination provides an efficient image acquisition strategy to not only reduce the number of acquired images but also reduce the exposure time by three quarters because it provides twice the illumination luminance. In the iteration process, each acquired intensity accounts for two centrosymmetric sub-apertures in the Fourier domain, resulting in faster spectrum filling. As a result, the hybrid coherent and incoherent illumination scheme exponentially reduces the number of acquired images while maintaining the wide spectrum coverage.

3.2. Efficient Synthetic Aperture Iteration Reconstruction

Figure 3 shows the flow chart of the iteration reconstruction, which is a modified version of the FPM algorithm to achieve efficient, high-quality synthetic aperture reconstruction for phase-less samples. Based on the characteristics of coherent and incoherent imaging systems, the iteration reconstruction strategy of ESA-FPM is implemented by separating the filter function corresponding to the bright-field and dark-field illuminations. At the beginning of the reconstruction, the bright-field image is used as an initial guess, which provides a close solution to accelerate the convergence. During each iteration, the sub-aperture spectrum corresponding to the bright-field illumination is extracted and its amplitude is updated by the bright-field measurement. The spectrum filtering function is defined as OTF instead of CTF to conform to incoherent imaging. Without sub-aperture scanning, one update fills the spectrum with 2× the coherent diffraction bandwidth of the objective lens. For dark-field illumination, the same dark-field intensity measurement is filtered by CTF (pupil function) to sequentially update two sub-apertures (sub-aperture 1 and sub-aperture 2) of the centrosymmetric distribution. To avoid the non-convex problems getting stuck in the local minima, we use an adaptive step-size strategy to gradually diminish the updating weight as the iteration accumulates.[56] At the end of this iteration recovery process, the converged solution in Fourier space will typically cover significantly extended-spectrum support with faster and stabilized convergence speed. Finally, the desired high-resolution result can be recovered with the wide FOV of the original image (low-magnification objective lens) as well as the resolution of the equivalent NA (the sum of the objective NA_{obj} and the illumination NA_{ill}).

To illustrate the information transfer characteristics, the OTF and CTF corresponding to the bright-field (incoherent) and dark-field (coherent) illuminations are shown in Figure 3. For the iteration update under coherent illumination, CTF is equivalent to the pupil function of the objective lens (without considering the aberration), which indicates that the original image is filled into Fourier space with a constrained aperture with the cut-off frequency of $\frac{NA_{obj}}{\lambda}$. The extended light source collects the bright-field image in an incoherent manner, and the OTF allows twice the bandwidth coverage of the coherent case in Fourier space. As a result, ESA-FPM can update the sample information within the bright-field bandwidth in a single acquisition and iteration. In
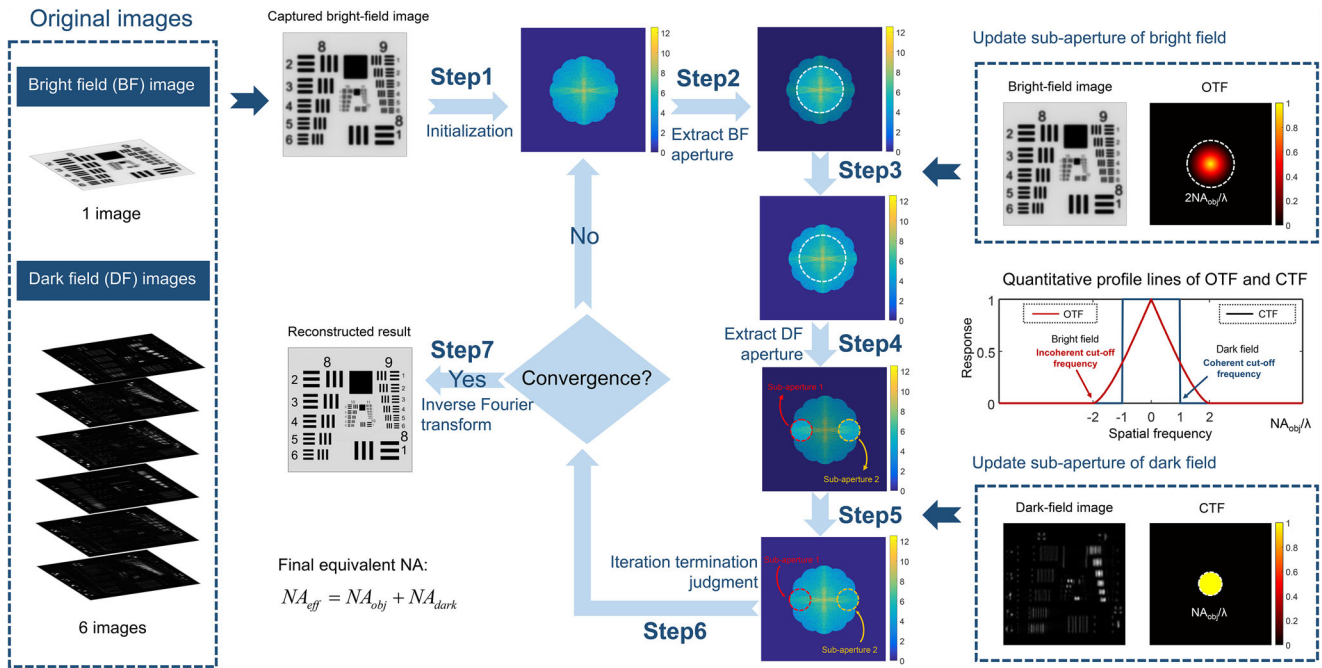
**ADVANCED
SCIENCE NEWS**

www.advancedsciencenews.com

LASER
& PHOTONICS
REVIEWS

www.lpr-journal.org

Figure 3. The flow chart of the iteration reconstruction of ESA-FPM.

addition, to overcome the poor contrast caused by weak OTF response, an additional deconvolution operation compensates for the updated sub-aperture spectrum by deconvoluting the bright-field intensity spectrum with the OTF, thereby enhancing the imaging resolution and contrast of the bright-field information. Furthermore, these weakened frequency components are also compensated and enhanced by the iteration of dark-field images. Consequently, the synthetic spectrum bandwidth is extended to the cut-off frequency the synthetic NA ($\frac{\text{NA}_{\text{obj}}+\text{NA}_{\text{ill}}}{\lambda}$) determined by the sum of the illumination NA_{ill} and objective lens NA_{obj}.

3.3. Data Redundancy Analysis and Efficiency Optimization

In FPM, the AP algorithm recovers the high-resolution information of the sample by continuously imposing constraints on the estimated value to make it gradually approach the correct solution. Redundant raw data is required in this process so that the iteration can reach a stable and reliable solution (the constraints resulting from the overlapping condition and the intensity measurements are satisfied simultaneously).[43,50] In Fourier space, the spectrum overlapping percentage R_{overlap} of sub-aperture spectrums corresponding to adjacent LED units is defined to describe the data redundancy. Several studies have demonstrated that a minimum spectrum overlapping percentage of 40% between the Fourier space areas of neighboring LEDs is needed to guarantee a reasonable and convergent result.[45,50] This sampling criterion can be used to design sparse illumination schemes to reduce the number of acquired images in FPM.

To eliminate data redundancy that delays algorithm time and only leave those data that ensure robust convergence of the algorithm, we further analyzed the data redundancy for ESA-FPM to achieve efficiency optimization. In our analysis, the minimum

spectrum overlapping percentage is determined to be 40% to ensure successful reconstruction. With the goal of achieving the maximum illumination NA with the least amount of acquired data, the spectrum overlapping percentage is analyzed from two aspects. A similar analysis can be applied to more illumination NAs to achieve a higher imaging resolution. First, the maximum synthetic NA is explored by analyzing the spectrum overlapping percentage under bright-field illumination and dark-field illumination with different NAs, the computational model of which is shown in **Figure 4**a. Its mathematical expression is too complicated, so a numerical simulation method is adopted in this case. To facilitate our analysis, we define a dark-field illumination coefficient S_{dark}, which determines the spectrum overlapping percentage

$$S_{\text{dark}} = \frac{\text{NA}_{\text{dark}}}{\text{NA}_{\text{obj}}} \tag{8}$$

where NA_{dark} is the NA of centrosymmetric sampling illumination. From this equation, S_{dark} is illustrated as the ratio of NA_{dark} to NA_{obj}, and it determines the final synthetic spectrum bandwidth. With the single annular dark-field illumination in our analysis, the highest frequency of the ESA-FPM can reach $\frac{(1+S_{\text{dark}})\text{NA}_{\text{obj}}}{\lambda}$. In a determined hardware setup (with a selected objective lens), a larger S_{dark} means a wider imaging bandwidth, which will achieve higher lateral resolution, however, the spectrum overlapping percentage decreases linearly. Until S_{dark} increases to 3, the sub-apertures of bright field and dark field are completely separated without any overlapping coverage.

We simulated the varying trend of the spectrum overlapping percentage with different S_{dark}, and the results are shown in Figure 4. Here, S_{dark} is chosen to be varying values from $\approx 1-3$. $S_{\text{dark}} \geq 1$ is determined to enable the ESA-FPM to achieve a
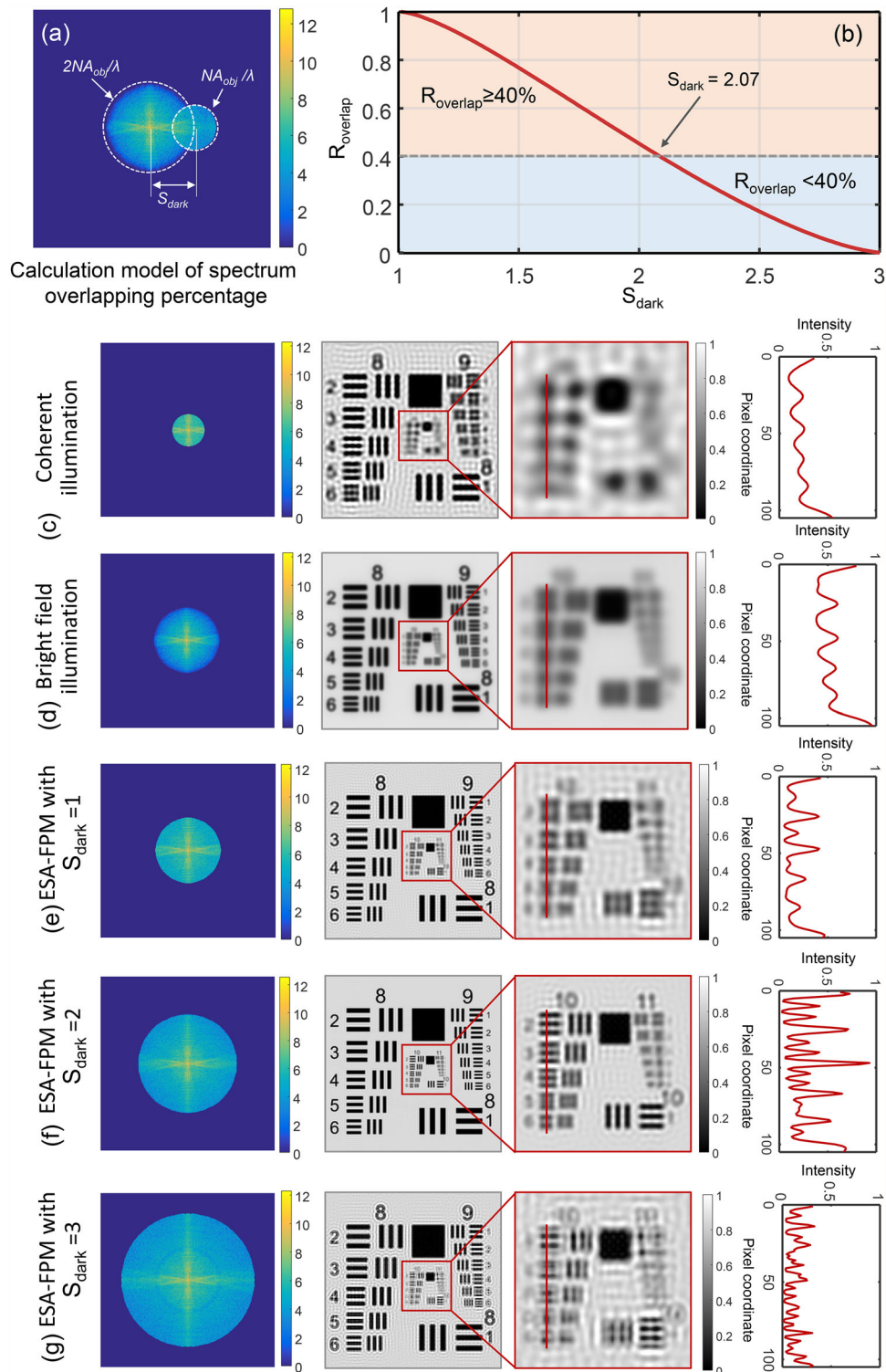
Figure 4. The simulation results of spectrum overlapping percentage with different dark-field illumination coefficients S_{dark} (it determines the maximum synthetic NA). a) The calculation model of spectrum overlapping percentage for sub-apertures of bright-field and dark-field illuminations. b) The numerical curve of spectrum overlapping percentage with the varying of S_{dark}. c–g) The simulation results of different illuminations with coherent illumination, bright- field illumination, and S_{dark} = 1, 2, 3.

ADVANCED
SCIENCE NEWS
www.advancedsciencenews.com

LASER
& PHOTONICS
REVIEWS
www.lpr-journal.org

diffraction limit beyond that of conventional bright-field microscopy. In Figure 4b, we plot the numerical curve of spectrum overlapping percentage with the varying of S_{dark}. It can be seen that when the dark-field illumination coefficient S_{dark} is less than 2.07, the spectrum overlapping percentage of the bright and dark fields is greater than or equal to 40%, which is considered to obtain an expected reconstruction result. Figure 4c–g display the reconstruction results and their enlarged images under different imaging approaches. As shown in Figure 4c, the central LED produces coherent illumination, thus forming an intensity image with a limited imaging resolution of $\frac{\lambda}{NA_{obj}}$. By opening the illumination aperture, bright-field illumination improves lateral imaging resolution (Figure 4d). Notice that although the theoretical bandwidth limit of the bright field reaches $\frac{2NA_{obj}}{\lambda}$, the imaging contrast deteriorates instead, resulting in the high-frequency details of the sample cannot be distinguished. The reason lies in that the OTF exhibits poor transmission response at high frequencies. Figure 4e–g display the reconstruction results of the ESA-FPM under different dark-field illumination coefficients with $S_{dark} = 1, 2, 3$, respectively. From Figure 4e, when the dark field illumination coefficient $S_{dark} = 1$, ESA-FPM exhibits more high-frequency details than the bright-field image with the same imaging bandwidth (Figure 4d). This is because the updates of the centrosymmetric sampling apertures of ESA-FPM compensate for the frequency components that are weakened by the system OTF (approaching $\frac{2NA_{obj}}{\lambda}$), leading to a significantly enhanced imaging contrast. When S_{dark} is set to 2 to satisfy the spectrum overlapping percentage of slightly greater than 40% (Figure 4f), the synthetic spectrum is significantly expanded while ensuring the correct reconstruction of the results. With the further increase in S_{dark}, a larger $S_{dark} = 3$ causes the frequency loss of the synthetic spectrum, resulting in a corrupted reconstruction result, as shown in Figure 4g. This is consistent with what is predicted in Figure 4b, where the unsatisfied spectrum overlapping percentage leads to incorrect imaging results. Therefore, ESA-FPM with $S_{dark} = 2$ can be considered as the optimal illumination under single-annulus dark-field illumination, which not only ensures the convergence of ESA-FPM iteration but also obtains the theoretical imaging resolution.

Then, aiming to confirm the minimum number of captured images, the sampling requirement of centrosymmetric sparse illumination is analyzed by numerical simulation and comparison. For this purpose, the LEDs are considered to be uniformly distributed in different azimuth angles on a dark-field illumination annulus with $S_{dark} = 2$. **Figure 5**a shows the calculation model of the spectrum overlapping percentage $R_{overlap}$ of dark field sub-apertures, which can be expressed as

$$R_{overlap} = 1 - \frac{2}{\pi}\arcsin[S_{dark}\sin(\frac{\pi}{2N})]$$
$$- \frac{2}{\pi}S_{dark}\sin(\frac{\pi}{2N})\sqrt{1 - [S_{dark}\sin(\frac{\pi}{2N})]^2} \qquad (9)$$

where N is the sampling number of centrosymmetric illumination. Since two LEDs are lit simultaneously for each acquisition, N illumination samples imply $2N$ dark-field sub-apertures. This equation can be used to calculate the spectrum overlapping percentage for different numbers of samples on an arbitrary illu-

mination NA. Figure 5b displays the varying numerical curve of the spectrum overlapping percentages with different sampling numbers N. Similarly, the 40% spectrum overlapping percentage is used as a criterion to define the minimum number of illumination sampling. Obviously, a larger N, which indicates a growing spectrum overlapping percentage, generates a better Fourier space coverage. The appropriate value of N can be determined by analyzing the quantization curve of Figure 5b. It can be seen that considering a sufficient spectrum overlapping percentage greater than 40%, then the value of N should be set to $N \geq 6$. To demonstrate and compare the reconstruction results of different N values, we further show the simulation results corresponding to N values of $N = 2, 4, 6, 8,$ and 10 in Figure 5c–g. As can be seen, a small N value of $N = 2$ or $N = 4$ leads to excessively sparse sampling, and the overlapping of sub-apertures cannot guarantee the convergence of iteration, resulting in obvious distortion. As expected, when N is increased to greater than 6, sufficient spectrum overlapping is obtained to recover a reliable reconstruction result. The resulting reconstructed image correctly shows the details of the sample without any distortion. Therefore, the minimum number of dark-field acquisitions of ESA-FPM to obtain a stable iteration reconstruction should be set to 6. It can be concluded that ESA-FPM achieves an imaging bandwidth of $\frac{3NA_{obj}}{\lambda}$ requiring only seven images (one bright-field image and six dark-field images).

4. Experiment Results

4.1. Resolution Validation Experiment of ESA-FPM Platform

The advantage of ESA-FPM is that only seven images are used to achieve high-throughput imaging, ensuring a wide imaging FOV with significantly improved resolution. In order to verify the imaging performance of the ESA-FPM, we conducted an experiment on a standard USAF resolution target and compared the reconstruction results of different imaging methods, including coherent imaging (center point illumination), bright field (incoherent imaging), FPM, and ESA-FPM. The experimental platform is built based on an existing commercial microscope, and its details can be found in Section 6. **Figure 6** displays the observation results in different imaging approaches including coherent imaging, bright-field imaging, FPM, and ESA-FPM to compare their imaging resolution. Figure 6a shows the full FOV image captured under the center LED illumination, exhibiting the lateral resolution of the original acquired image in FPM. A region of interest (ROI) is selected and zoomed in to explore the capabilities of imaging high-resolution detail of these methods. In Figure 6b, we give the data requirements and imaging throughput of these methods to compare their cost-efficiency. As expected, ESA-FPM achieves the optimal imaging performance with the least amount of data compared to other imaging methods. The imaging spectrum and visualized results of the different methods are then shown in Figure 6c,d. From Figure 6c, the expansion of the spectrum bandwidth by opening illumination is limited to no more than $\frac{2NA_{obj}}{\lambda}$, while FPM and ESA-FPM techniques break this limit. Furthermore, our ESA-FPM achieves the most efficient imaging while retaining the FPM's capability in spectrum expansion. The final imaging results and their enlarged
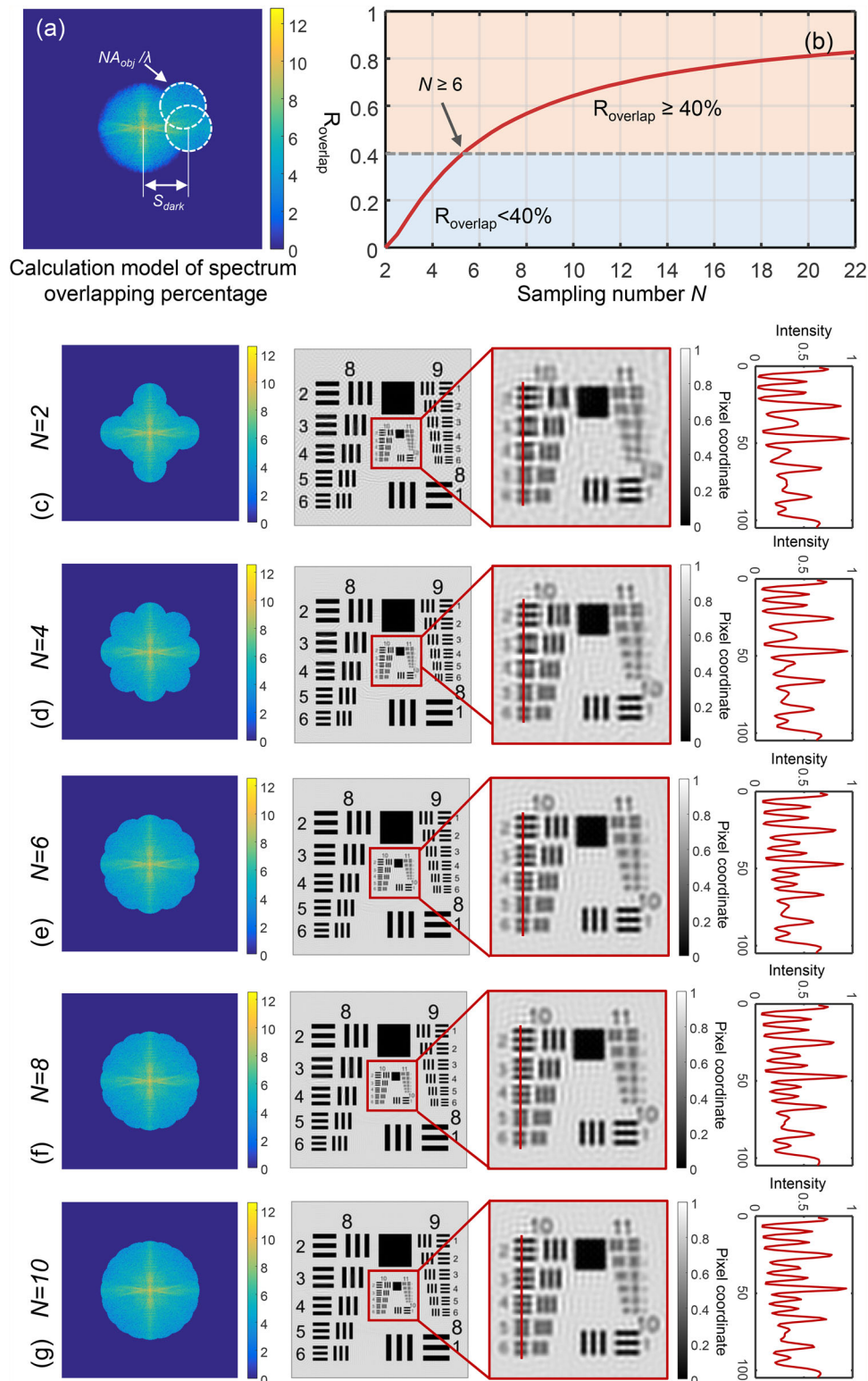
ADVANCED
SCIENCE NEWS

www.advancedsciencenews.com

LASER
& PHOTONICS
REVIEWS

www.lpr-journal.org

Figure 5. The simulation results of spectrum overlapping percentage with the sampling number of sparsely centrosymmetric illuminations (the number of the captured images). a) The calculation model of spectrum overlapping percentage for sub-apertures of dark-field illuminations. b) The numerical curve of spectrum overlapping percentage with the sampling number of the centrosymmetric dark field illuminations. c–g) The simulation results of different sampling numbers N of $N = 2$, $N = 4$, $N = 6$, $N = 8$, and $N = 10$.
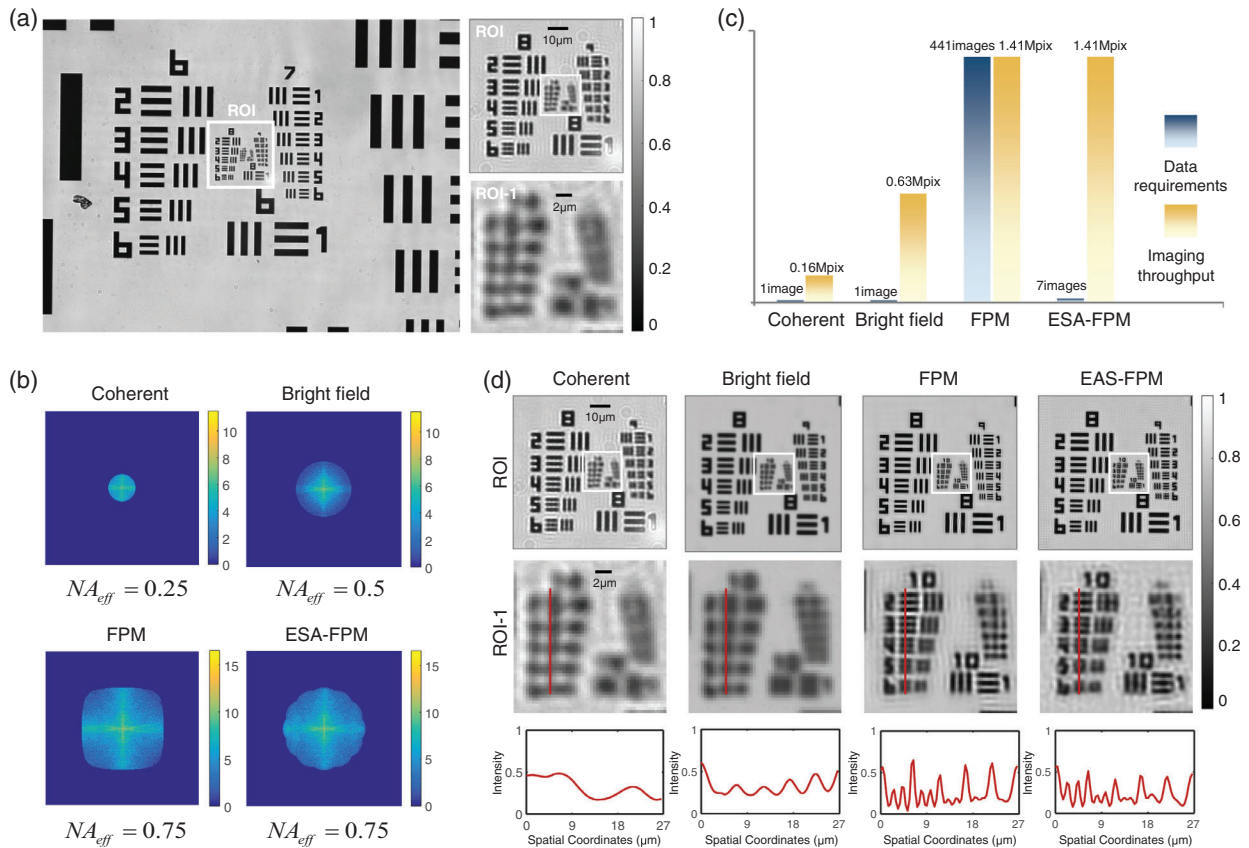
Figure 6. Experiment results of standard USAF resolution target under different imaging methods. a) Full FOV of the original image and a ROI under coherent illumination (center LED illumination). b) Comparisons of imaging data requirements and imaging throughput of different imaging methods. c) Imaging spectrums of the four methods and their equivalent NA, NA_{eff}. d) The experiment result of these four imaging methods.

ROI can be clearly observed in Figure 6d. The raw image under the bright-field illumination whose illumination NA_{ill} matching the objective NA_{obj} is collected by using the same objective lens. The extended illumination aperture achieves higher imaging resolution that approaches to $\frac{\lambda}{2NA_{obj}}$ (full-pitch resolution), but inevitably leads to compromised phase contrast especially for high spatial frequencies. Using sequential LED illumination to acquire images under traditional FPM, 441 images are used to reconstruct a high-throughput result with significantly improved resolution of 776 nm (full-pitch resolution of Group 10, Element 3), which is consistent with the theoretical full-pitch resolution. In contrast, ESA-FPM requires only seven acquired images to achieve the same spectrum bandwidth as conventional FPM. From Figure 6d, it achieves the comparable lateral resolution of 776 nm (0.75 NA resolution) as conventional FPM, with high-spatial-frequency features being reconstructed clearly. However, ESA-FPM requires only 1.6% of image data compared to conventional FPM.

4.2. High-Throughput Pathology Experiment Using Miniaturized ESA-FPM System

Pathological diagnosis requires the rapid acquisition of full FOV high-resolution images of pathological slides for accurate screen-

ing of lesion cells. The capabilities of rapid data acquisition and reconstruction of ESA-FPM provide a timely and effective realization for pathological diagnosis. Based on the ESA-FPM solution in Section 3.3, a miniaturized high-throughput ESA-FPM system with customized objective lens and LED is built for practical pathology diagnostic applications, as shown in Figure 9. An experiment was conducted using a pathological sample of Lymph node metastatic in squamous cell carcinoma, which is derived from a patient who signed a voluntary consent. In the prior sample preparation process, this pathological sample is routinely processed by hematoxylin-eosin (HE) staining, thus showing a colored distribution of strong absorption. The visualized results under different imaging approaches are shown in **Figure 7**. Under the conventional bright-field microscopic observation method, the original bright-field image (Figure 7a) shows limited discernible information. We select a ROI (marked by the white box in Figure 7a) to compare the distinguishable details under coherent imaging (central point illumination), bright-field imaging, and ESA-FPM, respectively. As shown in Figure 7b, compared to the other two methods, ESA-FPM yields visualized results with significantly enhanced resolution. Some tissue structures, such as blood cells and lymphocytes, that could not be resolved in the bright-field image can be clearly distinguished. Also, the nucleus of tissue is reconstructed correctly, while the details of lymphocytes are revealed clearly. In order to compare our
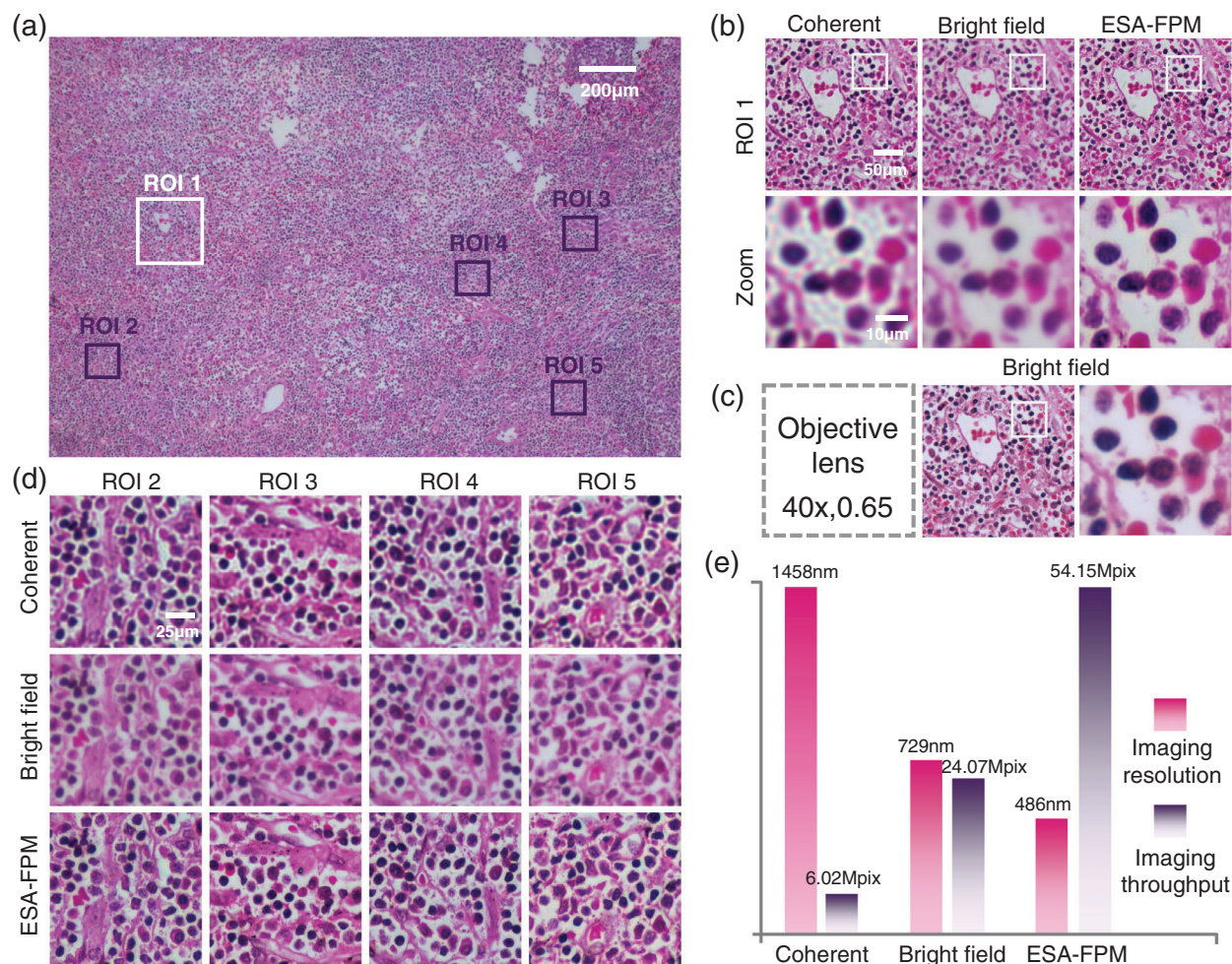
**ADVANCED
SCIENCE NEWS**

www.advancedsciencenews.com

LASER
& PHOTONICS
REVIEWS

www.lpr-journal.org

Figure 7. Experiment result of ESA-FPM on pathological sample of Lymph node metastatic in squamous cell carcinoma. a) Full FOV bright-field image with our customized objective lens (a magnification of 6× and a NA of 0.35). b) Zoom images of the ROI in the white box (ROI 1). c) The imaging result in conventional bright-field microscope using an objective lens with a magnification of 40× and a NA of 0.65. d) Comparison of the visualization results of ROIs (ROI 2, ROI 3, ROI 4, ROI 5) of coherent illumination, bright-field illumination, and ESA-FPM. e) Comparison of imaging resolution and throughput of coherent illumination, bright-field illumination, and ESA-FPM.

recovery results with those of conventional imaging using a high-magnification objective lens, we used an objective lens with 40×, 0.65 NA to observe the same pathological sample, and Figure 7c shows the visualized results corresponding to ROI 1. Thanks to the wide FOV of the original acquisition, the single image acquisition process of ESA-FPM obtained comparably high-quality imaging results across a FOV of 2.19×1.46 mm², which is 44.5 times larger than that of 40× objective lens. Meanwhile, our ESA-FPM realistically reconstructs the color absorption distribution of the sample and recovers more high-resolution information, obtaining sharper sample details compared to the 0.65 NA objective lens. Furthermore, four different ROIs are enlarged in Figure 7d, presenting the same high-quality reconstruction results for the entire wide FOV. As a result, the imaging throughput of ESA-FPM is increased exponentially compared to conventional bright-field imaging (from Figure 7d). It suggests that the high-throughput and high-resolution capabilities of ESA-FPM allow for statistically and biologically specific lesion analysis.

5. Conclusion and Discussion

In this paper, we proposed ESA-FPM, which adopts a new hybrid illumination scheme that joints the incoherent imaging (bright field) and coherent imaging (dark field), to enable the maximum data cost efficiency of FPM. In bright-field image acquisition, all LEDs are lit simultaneously to collect a single image, while dark-field images are acquired based on centrosymmetric sparse illumination sampling. Accordingly, the single bright field intensity iteratively updates a spectrum coverage with the 2× bandwidth of coherent diffraction limit, and each dark-field image covers both sub-aperture spectrums simultaneously. Furthermore, we analyzed the data redundancy of ESA-FPM through numerical simulations, giving the optimal ESA-FPM that achieves maximum data cost efficiency. As a result, using a bright-field illumination and dark-field illuminations with the illumination $NA_{dark} = 2NA_{obj}$, only seven images need to be collected in ESA-FPM to achieve an imaging bandwidth of $\frac{3NA_{obj}}{\lambda}$. We built a customized
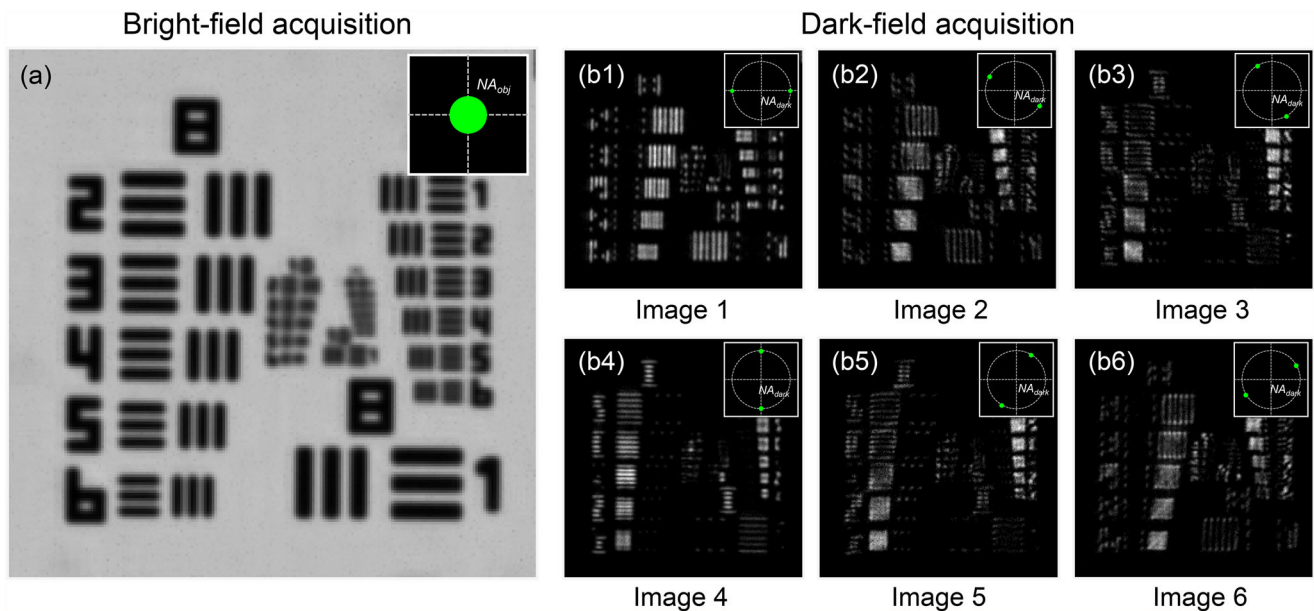
Figure 8. Raw images acquired by ESA-FPM method. a) Original bright-field acquisition. b1–b6) Original dark-field acquisitions.

miniaturized ESA-FPM system for pathology applications, which is equipped with an in-house designed low-magnification, high-NA objective lens and a high-brightness LED array. The experiment on the pathological sample indicates that ESA-FPM achieves a stable high-throughput imaging application with the least data collection.

We focused on analyzing the ESA-FPM for single-annulus dark-field illumination, that is, the case where only a dark-field illumination NA_{dark} exists. In fact, ESA-FPM can be used with more dark-field illumination NAs to achieve higher imaging resolution and larger imaging throughput. The analytical approach in this paper allows exploring the minimum data requirements under different synthetic NA for diversified pathology applications. Moreover, it must be stated that ESA-FPM is applicable for high-speed and high-throughput imaging of weak phase samples, for example, pathology samples. This is attributed to the fact that the centrosymmetric illumination of the bright field completely cancels out the transfer response of the phase transfer function (the phase transfer function shows an odd function distribution with the illumination function). For the high-throughput application of pathology diagnosis, the absorption needs to be imaged rather than the phase information as a priori for diagnosis. Therefore, ESA-FPM will provide a powerful high-throughput imaging technique for the application of pathology diagnosis. In contrast, quantitative phase imaging, which extracts the quantitative phase information of weakly absorptive samples in a non-invasive manner,[57,58] achieves the exact opposite purpose of our ESA-FPM. For phase imaging, asymmetric illuminations should be used to produce phase contrast and render phase information visible.[59,60] Asymmetric matched annular illumination has been demonstrated to be essential for improving the low-frequency phase contrast and enhancing the data acquisition efficiency, making high-speed quantitative phase imaging of unlabeled biological cells possible.[61] How to extend ESA-FPM to

image both amplitude and phase components of general samples is one interesting direction for future work.

6. Experimental Section

High-Throughput ESA-FPM Platform Based on a Commercial Microscope: A commercial microscope (Olympus, IX83) is used to construct the experimental system, which only needs a simple system modification by replacing traditional light sources with a 21 × 21 programmable LED array (with central wavelengths of 632, 525, and 460 nm). The spacing unit of LED is 4 mm, and it is placed 74 mm above the platform. The 89 LED units in the center are covered by gross glass to produce continuous uniform bright-field illumination. The programmable LED array is controlled by a custom-designed field-programmable-gate-array-based controller (Altera EP4CE10E22C8N), providing a high LED illumination pattern refresh rate (>1 kHz) and high display color-scale (8-bit grayscale for RGB channels). An objective lens with 10×, NA 0.25 is equipped to collect original images. In the implementation of FPM, illumination scanning with such a configuration acquired 441 images, extends spectrum bandwidth with a cutoff frequency of $\frac{3NA_{obj}}{\lambda}$. During image acquisition, the forming intensity images are ultimately recorded by a camera sensor with 1280×960, and a pixel size of 3.75 μm (the imaging source, DMK 23U445).

With such an experimental platform, the data acquisition process for the ESA-FPM could be described in two steps. First, all the bright-field LEDs are lit simultaneously to illuminate the sample, recording a bright-field image with an exposure time of 30 ms (**Figure 8**a). Next, the centrosymmetric LEDs on the illumination annulus of the matched $2NA_{obj}$ are lit simultaneously to acquire several dark-field images (Figure 8 b1–b6). Due to the double increase in radiant brightness under such centrosymmetric illumination, the dark-field image acquisition process of ESA-FPM could be completed in ≈1.5 s. Conventional FPM requires sequential illumination to acquire 441 images for the same imaging throughput, and the whole process is completed in ≈3 min. The raw datasets are used to perform the conventional FPM and the proposed ESA-FPM, respectively, to compare their reconstruction results. In the iteration reconstruction, each full-FOV raw image (1280 × 960 pixels) is divided into 6 × 4 sub-regions (256 × 256 pixels each), with a certain pixel overlap on each side

of neighboring subregions. Using a desktop computer (Intel i7 CPU), the algorithm processing time of conventional FPM for each sub-region is ≈30 s; however, this takes only 1 s in the ESA-FPM algorithm.

Miniaturized High-Throughput ESA-FPM System: A specialized ESA-FPM system is designed and built to enable efficient and high-throughput applications and its hardware configuration is shown in **Figure 9**. Figure 9a,b show the system schematic, where the key devices are the high-throughput objective lens and a customized LED array. As shown in Figure 9d, a customized discrete high-brightness LED array (central wavelength of 632, 510, and 460 nm) is placed on a lateral displacement platform 36 mm away from the carrier table. In accordance with the hybrid illumination modes, this LED is designed with nine LEDs gathered in the center region to produce incoherent illumination for bright field, and 12 LEDs evenly distributed in the outer annulus away from the center LED of 40 mm to implement centrosymmetric discrete illumination for dark field. The center LED is aligned on the system's optical axis to ensure the accuracy of the illumination angle. When acquiring images, an illumination diffuser (gross glass) is mounted on top of the bright-field LEDs to obtain a continuous illumination distribution. Under such illumination parameters, the illumination NA_{ill} generated by the maximum angle illumination is determined as 0.7. In order to unleash the optimal imaging performance of ESA-FPM, a high-throughput objective lens is designed with a magnification of 6× and a NA of 0.35, as shown in Figure 9c. Its internal optical structure is shown in Figure 9f. So the acquired images are endowed with both a larger imaging FOV (smaller magnification) and a higher resolution (higher NA_{obj}) compared to the general commercialized objective lenses. The above parameter configurations match the most efficient hybrid coherent/incoherent illumination concluded in Section 3.3, that is, $NA_{dark} = 2NA_{obj}$. In the imaging plane, a wide FOV sensor with a size of 5472 × 3648 and a pixel size of 2.4 µm (the imaging source DFK 33UX183) is adopted to acquire the original images. As a result, when ESA-FPM is implemented in this system, the reconstruction result could be achieved with a wide imaging FOV of 2.19 × 1.46 mm² and an imaging resolution of 486 nm (full-pitch resolution), leading to an imaging throughput with SBP of 54.15 Mpix.

Appendix: Information Symmetry Property of Centrosymmetric Dark-Field Illumination

Dark-field imaging exclusively collects scattered light from the sample, so the image intensity is no longer linearly dependent on sample distribution, as is a bright-field microscope image. To discuss the image formation model for centrosymmetric illumination of the dark field, the approximation method must be introduced to linearize the imaging model to obtain a tractable solution. Consider preparing a pathological sample, it is usually sliced into thin layers of tissue no more than 5 µm thick and processed with hematoxylin-eosin (HE) staining. Such a sample distribution can be characterized by the weakly phase object approximation model, whereby the complex distribution of the pathological sample can be expressed as $t(x, y) \approx 1 + a(x, y) + i\phi(x, y)$. In addition, this approximation model is also consistent with the observation concern of pathological samples, whose absorption rather than phase is used as an important basis for the diagnosis of pathology applications. In order to analyze the image information in the Fourier domain, we take the Fourier transform on the complex distribution of the sample and obtain its Fourier spectrum

$$T(u, v) \approx \delta(u, v) + A(u, v) + i\Phi(u, v) \tag{10}$$

where $\delta(u, v)$ is the Dirac Delta function, which denotes the direct current (DC) component, $A(u, v)$ and $\Phi(u, v)$ represent the amplitude and phase spectrum distribution of the sample, respectively.

When the sample is illuminated by an oblique dark-field illumination with the spatial frequency of (u_j, v_j) (for dark-field illumination, $\sqrt{|u_j|^2 + |v_j|^2} > \frac{NA_{obj}}{\lambda}$), the limited sub-aperture spectrum will be shifted so that the zero-frequency component moves out of the diffraction bandwidth of the objective lens, only transmitting the scattered light of the sample. Thus, the spectrum distribution before the camera plane can be denoted as the distribution of the shifted by (u_j, v_j) and low-pass filtered by the pupil function $P(u, v)$

$$W_{u_j,v_j}(u, v) \approx [A(u - u_j, v - v_j) + i\Phi(u - u_j, v - v_j)]P(u, v) \tag{11}$$

Then, the intensity spectrum acquired by the camera can be represented as the convolution of the spectrum distribution of Equation (11) and its complex conjugate

$$I_{u_j,v_j}(u, v) \approx W_{u_j,v_j}(u, v) \otimes W^*_{u_j,v_j}(-u, -v)$$

$$= [A(u - u_j, v - v_j)P(u, v) + i\Phi(u - u_j, v - v_j)P(u, v)] \otimes \ldots$$

$$[A^*(-u - u_j, -v - v_j)P(u, v) - i\Phi^*(-u - u_j, -v - v_j)P(u, v)]$$

$$= [A(u - u_j, v - v_j)P(u, v)] \otimes [A(u + u_j, v + v_j)P(u, v)] + \ldots$$

$$[\Phi(u - u_j, v - v_j)P(u, v)] \otimes [\Phi(u + u_j, v + v_j)P(u, v)] + \ldots$$

$$i\{[A(u + u_j, v + v_j)P(u, v)] \otimes [\Phi(u - u_j, v - v_j)P(u, v)] - \ldots$$

$$[A(u - u_j, v - v_j)P(u, v)] \otimes [\Phi(u + u_j, v + v_j)P(u, v)]\} \tag{12}$$

where $\otimes$ is the convolution operators. Since both of $a(x, y)$ and $\phi(x, y)$ can be considered as real functions, $A^*(-u - u_j, -v - v_j)$ and $\Phi^*(-u - u_j, -v - v_j)$ in Equation (12) can be equated to $A(u + u_j, v + v_j)$ and $\Phi(u + u_j, v + v_j)$, respectively. Under a pair of centrosymmetric illuminations, the finite aperture will always be shifted with centrosymmetric spatial frequencies of (u_j, v_j) and $(-u_j, -v_j)$. Then, the dark-field intensity can be expressed as

$$I_{u_j,v_j}(u, v) + I_{-u_j,-v_j}(u, v) = 2[A(u - u_j, v - v_j)P(u, v)]$$

$$\otimes [A(u + u_j, v + v_j)P(u, v)] + \ldots 2[\Phi(u - u_j, v - v_j)P(u, v)]$$

$$\otimes [\Phi(u + u_j, v + v_j)P(u, v)] \tag{13}$$

From this equation, the cross-convolution terms of the absorption and phase are offset by each other, leaving only the self-convolution term of amplitude (absorption) and the self-convolution term of phase. The weak phase approximation usually considers samples with a small phase (usually less than 1 rad), then the self-convolution term of the phase can be omitted

$$I_{u_j,v_j}(u, v) + I_{-u_j,-v_j}(u, v) \approx 2[A(u - u_j, v - v_j)P(u, v)]$$

$$\otimes [A(u + u_j, v + v_j)P(u, v)] \tag{14}$$

Hence, we can conclude that under the weak phase approximation, the centrosymmetric illumination cancels the phase of the sample, and almost all contribution of the dark-field intensity originates from the amplitude (absorption) of the sample. Such a captured intensity image can be used to update both sub-apertures under centrosymmetric illumination. Consequently,
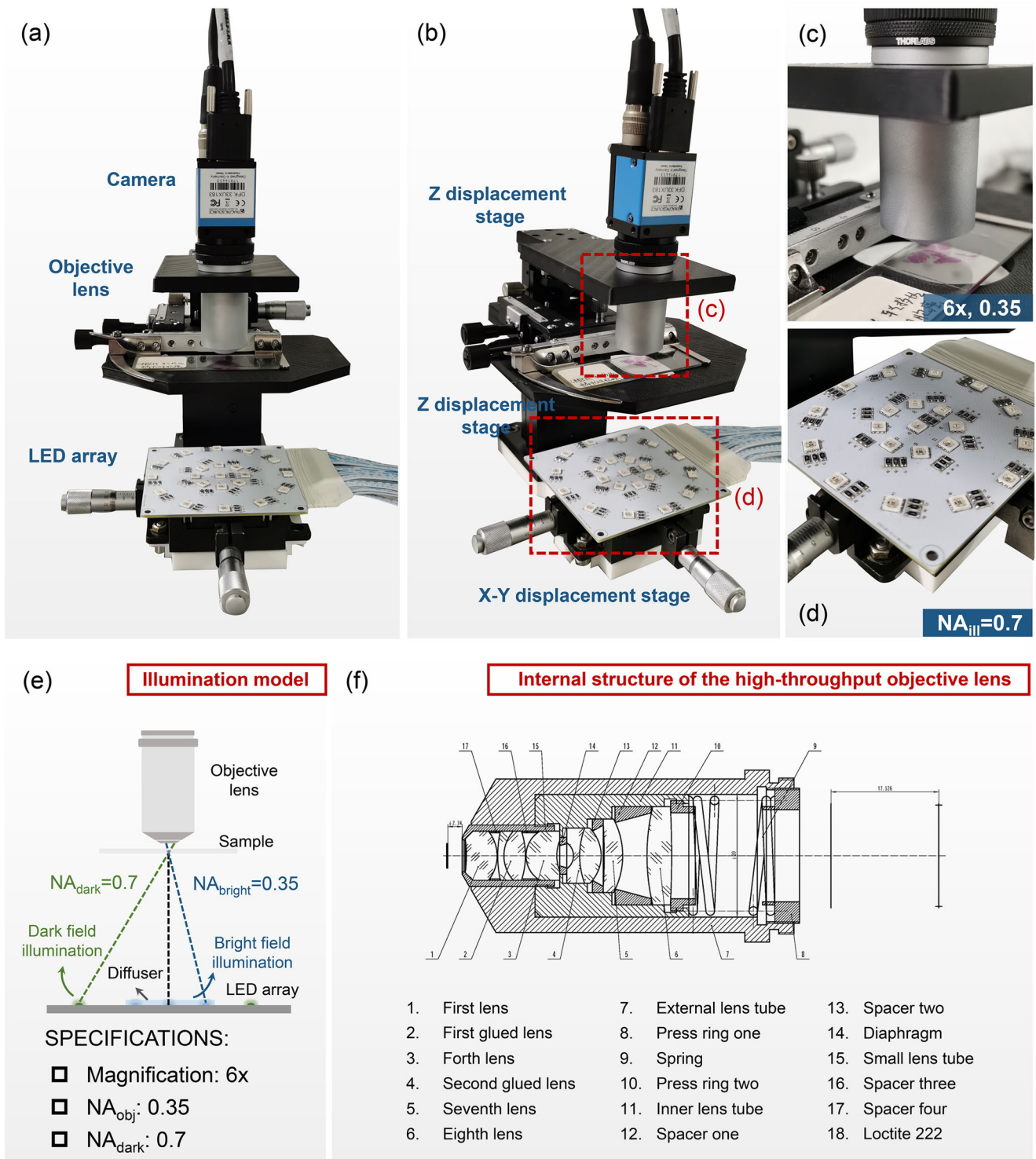
**ADVANCED
SCIENCE NEWS**

www.advancedsciencenews.com

www.lpr-journal.org

LASER
& PHOTONICS
REVIEWS

Figure 9. High-throughput ESA-FPM system. a,b) Hardware configuration of the ESA-FPM system. c) A customized objective lens with low magnification and high NA. d) A customized discrete high-brightness LED array matching our ESA-FPM. e) Schematic diagram of LED illumination. f) Details of the internal structure of the designed objective lens.
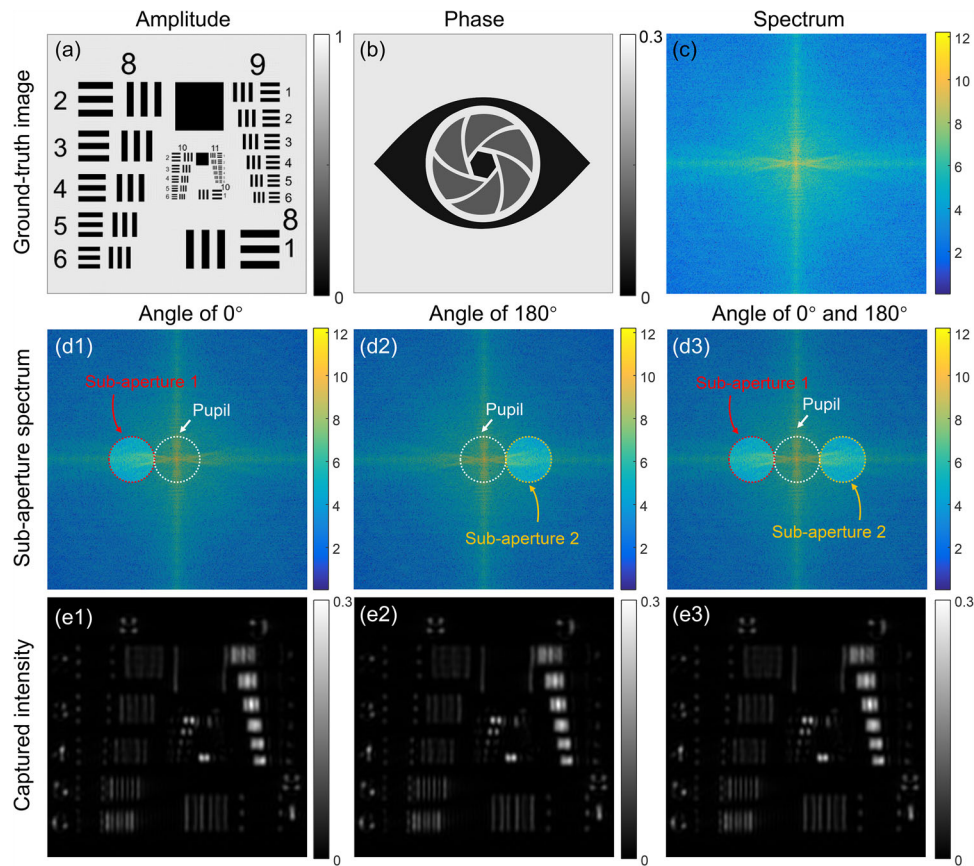
ADVANCED
SCIENCE NEWS
www.advancedsciencenews.com

LASER
& PHOTONICS
REVIEWS

www.lpr-journal.org

Figure A1. Simulation and comparison of intensity of centrosymmetric illumination. a,b) Ground-truth amplitude and phase images for simulation. c) Ground-truth high-resolution spectrum. d1–d3) Sub-aperture spectrums with illuminations of 0°, 180°, and simultaneous illumination at 0° and 180°. e1–e3) Captured intensities with illuminations of 0°, 180°, and simultaneous illumination at 0° and 180°.

the centrosymmetric dark-field illumination provides an efficient image acquisition strategy to not only reduce the number of images acquired but also save exposure time. In the iteration process, each acquired intensity allows for coverage of two sub-apertures in the Fourier domain, resulting in faster spectrum filling.

We used a numerical simulation to demonstrate the acquisition intensity of the centrosymmetric dark-field illumination. A realistic FPM system configuration with a microscope objective with NA_{obj} of 0.25 and the illumination NA_{ill} of 0.5 is used to generate dark field images under large angle oblique illuminations. The ground-truth complex distribution is created from the amplitude image shown in **Figure A1**a and the phase image shown in Figure A1b. In order to simulate the pathological section samples with strong absorption and weak phase, we set the range of amplitude from 0 to 1 and the phase from 0 to 0.3 rad. Figure A1c shows the simulated ground-truth spectrum, which will be used to generate the low-resolution dark-field measurements under centrosymmetric oblique illuminations by imposing shifted low-pass filters at the corresponding regions of the Fourier space. As shown in Figure A1d1,d2, the sub-apertures corresponding to the azimuths of 0° (sub-aperture 1) and 180° (sub-aperture 2), are extracted, respectively. Figure A1e1,e2 show their simulated intensity images, which both present a clear amplitude distribution with almost no visible phase distribution. We then sim-

ulated the intensity image of centrosymmetric illuminations of 0° and 180° by superimposing the intensity distribution corresponding to the spectrum of the two sub-apertures (sub-aperture 1 and sub-aperture 2 in Figure A1d3). Figure A1e3 shows the resulting intensity, which can only observe the amplitude distribution of the sample but ignores phase distribution. This is consistent with the derivation of Equation (14), that is, for samples with a weak phase, centrosymmetric dark-field illumination cancels the phase information of the sample so that only its amplitude information is recorded in the intensity image. Therefore, the captured intensity image acquired by the centrosymmetric illuminations can be used to simultaneously fill the two dark-field sub-aperture spectrums.

Acknowledgements

solutions for LED arrays. The authors also thank Ran Ye from Nanjing Normal University for proofreading the manuscript.

[1] A. C. Chan, J. Kim, A. Pan, H. Xu, D. Nojima, C. Hale, S. Wang, C. Yang, *Sci. Rep.* **2019**, *9*, 11114.
[2] V. Starkuviene, R. Pepperkok, *Br. J. Pharmacol.* **2007**, *152*, 62.
[3] E. Glory, R. F. Murphy, *Dev. Cell* **2007**, *12*, 7.
[4] F. Ghaznavi, A. Evans, A. Madabhushi, M. Feldman, *Annu. Rev. Pathol.: Mech. Dis.* **2013**, *8*, 331.
[5] L. Pantanowitz, *J. Pathol. Inf.* **2010**, *1*, 15.
[6] J. E. Greivenkamp, *Field Guide to Geometrical Optics*, Vol. *1*, SPIE press, Bellingham, WA **2004**.
[7] J. Ho, A. V. Parwani, D. M. Jukic, Y. Yagi, L. Anthony, J. R. Gilbertson, *Hum. Pathol.* **2006**, *37*, 322.
[8] D. Hamilton, C. Sheppard, *J. Microsc.* **1984**, *133*, 27.
[9] S. B. Mehta, C. J. Sheppard, *Opt. Lett.* **2009**, *34*, 1924.
[10] L. Tian, J. Wang, L. Waller, *Opt. Lett.* **2014**, *39*, 1326.
[11] G. Popescu, *Quantitative Phase Imaging of Cells and Tissues*, McGraw-Hill Education, New York, NY **2011**.
[12] Y. Park, C. Depeursinge, G. Popescu, *Nat. Photonics* **2018**, *12*, 578.
[13] G. Popescu, T. Ikeda, R. R. Dasari, M. S. Feld, *Opt. Lett.* **2006**, *31*, 775.
[14] R. Ling, W. Tahir, H.-Y. Lin, H. Lee, L. Tian, *Biomed. Opt. Express* **2018**, *9*, 2130.
[15] F. Tian, J. Hu, W. Yang, *arXiv:2101.07975*, **2021**.
[16] J. Oh, K. Lee, Y. Park, *Laser Photonics Rev.* **2021**, *16*, 2100559.
[17] C. Zuo, J. Li, J. Sun, Y. Fan, J. Zhang, L. Lu, R. Zhang, B. Wang, L. Huang, Q. Chen, *Opt. Lasers Eng.* **2020**, *135*, 106187.
[18] C. Zheng, D. Jin, Y. He, H. Lin, J. Hu, Z. Yaqoob, P. T. C. So, R. Zhou, *Adv. Photonics* **2020**, *2*, 065002.
[19] G. Zheng, R. Horstmeyer, C. Yang, *Nat. Photonics* **2013**, *7*, 739.
[20] A. Greenbaum, W. Luo, T.-W. Su, Z. Göröcs, L. Xue, S. O. Isikman, A. F. Coskun, O. Mudanyali, A. Ozcan, *Nat. Methods* **2012**, *9*, 889.
[21] A. E. Cetin, A. F. Coskun, B. C. Galarreta, M. Huang, D. Herman, A. Ozcan, H. Altug, *Light: Sci. Appl.* **2014**, *3*, e122.
[22] W. Bishara, T.-W. Su, A. F. Coskun, A. Ozcan, *Opt. Express* **2010**, *18*, 11181.
[23] T.-W. Su, S. Seo, A. Erlinger, A. Ozcan, *Biotechnol. Bioeng.* **2009**, *102*, 856.
[24] Y. Park, M. Diez-Silva, G. Popescu, G. Lykotrafitis, W. Choi, M. S. Feld, S. Suresh, *Proc. Natl. Acad. Sci. U. S. A.* **2008**, *105*, 13730.
[25] R. Horstmeyer, J. Chung, X. Ou, G. Zheng, C. Yang, *Optica* **2016**, *3*, 827.
[26] O. Mudanyali, D. Tseng, C. Oh, S. O. Isikman, I. Sencan, W. Bishara, C. Oztoprak, S. Seo, B. Khademhosseini, A. Ozcan, *Lab Chip* **2010**, *10*, 1417.
[27] S. Seo, T.-W. Su, D. K. Tseng, A. Erlinger, A. Ozcan, *Lab Chip* **2009**, *9*, 777.
[28] K. Lee, K. Kim, J. Jung, J. Heo, S. Cho, S. Lee, G. Chang, Y. Jo, H. Park, Y. Park, *Sensors* **2013**, *13*, 4170.
[29] H. Majeed, S. Sridharan, M. Mir, L. Ma, E. Min, W. Jung, G. Popescu, *J. Biophotonics* **2017**, *10*, 177.
[30] G. Zheng, C. Shen, S. Jiang, P. Song, C. Yang, *Nat. Rev. Phys.* **2021**, *3*, 207.
[31] A. J. Williams, J. Chung, X. Ou, G. Zheng, S. Rawal, Z. Ao, R. Datar, C. Yang, R. J. Cote, *J. Biomed. Opt.* **2014**, *19*, 066007.
[32] J. Chung, X. Ou, R. P. Kulkarni, C. Yang, *PloS One* **2015**, *10*, e0133489.
[33] J. Kim, B. M. Henley, C. H. Kim, H. A. Lester, C. Yang, *Biomed. Opt. Express* **2016**, *7*, 3097.
[34] R. W. Gerchberg, *Optik* **1972**, *35*, 237.
[35] J. R. Fienup, *Appl. Opt.* **1982**, *21*, 2758.
[36] H. M. L. Faulkner, J. Rodenburg, *Phys. Rev. Lett.* **2004**, *93*, 023903.
[37] J. M. Rodenburg, H. M. Faulkner, *Appl. Phys. Lett.* **2004**, *85*, 4795.
[38] A. M. Maiden, J. M. Rodenburg, *Ultramicroscopy* **2009**, *109*, 1256.
[39] S. Pacheco, B. Salahieh, T. Milster, J. J. Rodriguez, R. Liang, *Opt. Lett.* **2015**, *40*, 5343.
[40] J. Chung, H. Lu, X. Ou, H. Zhou, C. Yang, *Biomed. Opt. Express* **2016**, *7*, 4787.
[41] Y. Zhang, W. Jiang, Q. Dai, *Opt. Express* **2015**, *23*, 33822.
[42] O. Bunk, M. Dierolf, S. Kynde, I. Johnson, O. Marti, F. Pfeiffer, *Ultramicroscopy* **2008**, *108*, 481.
[43] S. Dong, R. Shiradkar, P. Nanda, G. Zheng, *Biomed. Opt. Express* **2014**, *5*, 1757.
[44] L. Tian, X. Li, K. Ramchandran, L. Waller, *Biomed. Opt. Express* **2014**, *5*, 2376.
[45] S. Dong, Z. Bian, R. Shiradkar, G. Zheng, *Opt. Express* **2014**, *22*, 5455.
[46] C. Kuang, Y. Ma, R. Zhou, J. Lee, G. Barbastathis, R. R. Dasari, Z. Yaqoob, P. T. So, *Opt. Express* **2015**, *23*, 26999.
[47] B. Lee, J.-y. Hong, D. Yoo, J. Cho, Y. Jeong, S. Moon, B. Lee, *Optica* **2018**, *5*, 976.
[48] A. Zhou, N. Chen, H. Wang, G. Situ, *J. Opt.* **2018**, *20*, 095701.
[49] L. Tian, Z. Liu, L.-H. Yeh, M. Chen, J. Zhong, L. Waller, *Optica* **2015**, *2*, 904.
[50] J. Sun, Q. Chen, Y. Zhang, C. Zuo, *Opt. Express* **2016**, *24*, 15765.
[51] P. C. Konda, L. Loetgering, K. C. Zhou, S. Xu, A. R. Harvey, R. Horstmeyer, *Opt. Express* **2020**, *28*, 9603.
[52] L.-H. Yeh, J. Dong, J. Zhong, L. Tian, M. Chen, G. Tang, M. Soltanolkotabi, L. Waller, *Opt. Express* **2015**, *23*, 33214.
[53] C. Yang, J. Qian, A. Schirotzek, F. Maia, S. Marchesini, *arXiv:1105.5628*, **2011**.
[54] E. Wolf, *J. Opt. Soc. Am. A* **1986**, *3*, 76.
[55] X. Ma, M. Yao, Z. Zhang, J. Peng, S. Li, J. Zhong, *IEEE Trans. Comput. Imaging* **2019**, *6*, 317.
[56] C. Zuo, J. Sun, Q. Chen, *Opt. Express* **2016**, *24*, 20724.
[57] G. Popescu, *Methods Cell Biol.* **2008**, *90*, 87.
[58] L. Tian, L. Waller, *Opt. Express* **2015**, *23*, 11394.
[59] Y. Fan, J. Sun, Q. Chen, X. Pan, L. Tian, C. Zuo, *Photonics Res.* **2019**, *7*, 890.
[60] Y. Baek, Y. Park, *Nat. Photonics* **2021**, *15*, 354.
[61] J. Sun, C. Zuo, J. Zhang, Y. Fan, Q. Chen, *Sci. Rep.* **2018**, *8*, 7669.